mater.scichina.com link.springer.com

Published online 29 September 2021 | https://doi.org/10.1007/s40843-021-1781-y
Sci China Mater 2022, 65(2): 451–459

High-sensitivity shortwave infrared photodetectors of metal-organic frameworks integrated on 2D layered materials

Fakun Wang, Jie Wu, Yue Zhang, Sijie Yang, Na Zhang, Huiqiao Li and Tianyou Zhai*

ABSTRACT **Photodetectors operating in the shortwave infrared region are of great significance due to their extensive applications in both commercial and military fields. Narrow-bandgap two-dimensional layered materials (2DLMs) are considered as the promising candidates for constructing next-generation high-performance infrared photodetectors. Nevertheless, the performance of 2DLMs-based photodetectors can hardly satisfy the requirements of practical applications due to their weak optical absorption. In the present study, a strategy was proposed to design high-performance shortwave infrared photodetectors by integrating metal-organic frameworks (MOFs) nanoparticles with excellent optical absorption characteristics and 2DLM with high mobility. Further, this study demonstrated the practicability of this strategy in a MOF/2DLM (Ni-CAT-1/Bi_2Se_3) hybrid heterojunction photodetector. Due to the transfer of photo-generated carriers from the MOF to Bi_2Se_3, the MOF nanoparticles integrated on the Bi_2Se_3 layer can increase the photocurrent by 2–3 orders of magnitude. The resulting photodetector presented a high responsivity of 4725 A W^{-1} and a superior detectivity of 3.5 × 10^{13} Jones at 1500 nm. The outstanding performance of the hybrid heterojunction arises from the synergistic function of the enhanced optical absorption and photogating effect. In addition, the proposed device construction strategy combining MOF photosensitive materials with 2DLMs shows a high potential for the future high-performance shortwave infrared photodetectors.**

Keywords: shortwave infrared photodetector, 2D layered materials, metal-organic frameworks, hybrid heterojunctions

INTRODUCTION

Shortwave infrared (SWIR) photodetector is one of the core components in modern electronics industry, which demonstrates a vital role in various fields such as military defense, industrial production, medical diagnosis and optical communication [1–5]. Two-dimensional layered materials (2DLMs) with narrow bandgap and high mobility are considered as the promising candidates for next-generation infrared optoelectronics due to their unique structures and photoelectric properties [6–11]. At present, considerable efforts have been devoted to demonstrating the SWIR photodetection performance of 2DLMs [1,5]. However, most of the 2DLMs-based SWIR photodetectors suffer from low responsivity (10^{-3}–10^{1} A W^{-1}) due to the intrinsic weak optical absorption induced by their atomically thin nature [5]. In photodetectors, the responsivity (R) is jointly determined by the external quantum efficiency (EQE) and the photoconductivity gain (G) according to the equation of $R = \frac{e\lambda}{hc} \times \mathrm{EQE} \times G$, where h, c, e and λ refer to the reduced Planck constant, light velocity, elementary electronic charge and incident wavelength, respectively. EQE is positively correlated with the optical absorption efficiency. As a result, the responsivity can be improved by enhancing optical absorption and introducing high photoconductivity gain. An effective strategy to achieve high responsivity is to combine a strong light absorption layer with high mobility 2DLMs [9,12]. In this configuration, the photosensitive layer absorbs photons and generates the electron-hole pairs under illumination. Then, the photo-generated carriers are transferred to the 2DLMs, thus enhancing the responsivity. In the meanwhile, part of the photo-generated carriers (electrons or holes) are captured by the traps or defects in the photosensitive layer and can form a photo-induced localized field (photogating effect). As a result, the carriers can recirculate repeatedly in the 2DLM channel before the recombination, further increasing the responsivity.

Currently, the selected photosensitive layers mainly contain plasmonic nanostructure [13,14], colloidal quantum dots (e.g., PbS, PbSe, HgTe) [12,15,16], low-dimensional perovskites [17–19], and inorganic nanoparticles [20,21]. For example, the HgTe-sensitized MoS_2 photodetector demonstrates an outstanding responsivity on the order of 10^3 A W^{-1} at a wavelength of 2 μm [15]. The hybrid Ti_2O_3 nanoparticles/graphene device achieves a high responsivity of 300 A W^{-1} in a broadband wavelength range up to 10 μm [20]. Even though these photosensitive materials have been effective on improving the responsivity of 2DLM-based photodetectors, they still have some shortcomings in practical applications. The enhancement of plasmonic nanostructure is limited by its resonant frequency and the toxicity of colloidal quantum dots is harmful to human health. The instability of perovskite limits device applications, and the high dark current of inorganic nanoparticles will generate low detectivity. Therefore, it is of great significance to develop a promising photosensitive material that can overcome the above-mentioned drawbacks.

In the present work, a novel strategy was proposed by utilizing metal-organic frameworks (MOFs) nanoparticles as the photo-

State Key Laboratory of Materials Processing and Die & Mould Technology, School of Materials Science and Engineering, Huazhong University of Science and Technology, Wuhan 430074, China
* Corresponding author (email: zhaity@hust.edu.cn)

sensitive materials of 2DLM-based photodetectors. MOFs formed by the coordination of metal ions and organic ligands exhibit highly tailorable bandgap, optical absorbance and electrical conductivity through varying the metal, ligand, and/or the growth conditions [22–28], which can be applied to different situations in line with the requirements of detection bands. Among them, MOF (Ni-CAT-1) possesses a narrow bandgap of 0.48 eV and strong optical absorption in the SWIR region [29,30], making it appropriate to combine with 2DLM to achieve high-performance SWIR photodetection. In addition, the moderate electrical conductivity induced by the high porosity of MOF does not significantly increase the dark current, thus retaining the high detectivity of the device [24,29]. Consequently, we demonstrated the high-sensitivity SWIR photodetectors by hybridizing Ni-CAT-1 nanoparticles with high-mobility 2D Bi_2Se_3 flakes, where a high responsivity of 4725 A W^{-1} and a superior detectivity of 3.5×10^{13} Jones at 1500 nm were obtained in the present Ni-CAT-1/Bi_2Se_3 hybrid heterojunction. The outstanding performance can be attributed to the synergistic function of the enhanced optical absorption and photogating effect. The obtained results indicate the great potential of combining MOF materials with 2DLMs for high-performance infrared optoelectronic applications.

EXPERIMENTAL SECTION

Preparation of 2D Bi_2Se_3 flakes

The 2D Bi_2Se_3 flakes were obtained *via* van der Waals epitaxial growth in a horizontal single-zone furnace equipped with a quartz tube. Bi_2Se_3 powder (0.2 g) and fresh mica substrate were employed as the precursor and growth substrate, and were placed at the center and the downstream region of the furnace, respectively. The center region was heated up to 600°C over 30 min and maintained at 600°C for 45 min under 80 standard cubic centimeter per minute (sccm) Ar carrier gas flow. Then the furnace was naturally cooled down to room temperature, and then the high-quality 2D Bi_2Se_3 flakes were obtained on the mica substrates.

Synthesis of Ni-CAT-1 nanoparticles

In this study, 0.01×10^{-3} mol HHTP (2,3,6,7,10,11-hexahydroxytriphenylene) and 0.05×10^{-3} mol nickel acetate ($Ni(CH_3COO)_2$) were dissolved separately in deionized water by sonication to prepare stock solutions. Next, 3 mL of each stock solution was added into a 20-mL cylindrical pressure vial and Ni-CAT-1 nanoparticles were formed after heating the vial at 85°C for 12 h.

Fabrication of 2D Bi_2Se_3/Ni-CAT-1 hybrid heterojunction device

First of all, the as-grown 2D Bi_2Se_3 flakes on mica substrate were transferred onto a silicon wafer with 300 nm thermalized SiO_2 layer by the poly(methyl methacrylate) (PMMA) and poly(propylene carbonate) (PPC)-assisted transfer technique [31]. Afterwards, the Bi_2Se_3-based back-gate field-effect transistor was fabricated by the standard electron beam lithography (ELPHY Plus, Raith GmbH) and thermal evaporation (Nexdep, Angstrom Engineering). Subsequently, the as-fabricated Bi_2Se_3 device was immersed in a mixture of HHTP and $Ni(CH_3COO)_2$ stock solution, and the Ni-CAT-1 nanoparticles self-assembled on the surface of Bi_2Se_3 flakes after heating at 85°C for 12 h. Finally, the Bi_2Se_3/Ni-CAT-1 hybrid heterojunction device was washed with deionized water for several times and annealed at 100°C for 10 min to remove the moisture.

Characterization and measurements

The phase and structure of the as-synthesized Ni-CAT-1 nanoparticles were determined by a powder X-ray diffractometer (XRD, D2 Phaser, Bruker) and transmission electron microscopy (TEM, Tecnai G2 F30, FEI). The morphology of the as-fabricated Bi_2Se_3/Ni-CAT-1 hybrid heterojunction was obtained by optical microscopy (BX51, OLYMPUS), atomic force microscopy (AFM, Dimension Icon, Bruker) and scanning electron microscopy (SEM, Quanta 650, FEI). Raman spectra were collected using a confocal microscope spectrometer (Alpha 300R, WITec) equipped with a 532-nm laser. Besides, the optical absorption spectra were recorded on an ultraviolet visible near-infrared spectrophotometer (SolidSpec-3700, SHIMADZU). The electrical measurements were conducted on a probe station (CRX-6.5K, Lakeshore), which was connected to a semiconductor analyzer (4200-SCS, Keithley). In terms of photodetection, the incident light with a variety of wavelengths was provided by a broadband laser-driven light source (EQ-1500, Energetiq).

RESULTS AND DISCUSSION

The schematic diagram of the proposed MOF/2DLM (Ni-CAT-1/Bi_2Se_3) hybrid heterojunction photodetector is displayed in Fig. 1a. It represents the configuration of 2D Bi_2Se_3 channel decorated with Ni-CAT-1 nanoparticles. Ni-CAT-1 exhibits a layered structure (Fig. 1b) and strong light absorption in the near-infrared region. As a result, it can be easily epitaxially grown on the surface of layered Bi_2Se_3 flakes and used as an efficient light absorber to enhance the light absorption capacity of the heterojunction device. As shown in Fig. 1c, incident SWIR light was absorbed by the MOF nanoparticles film under illu-

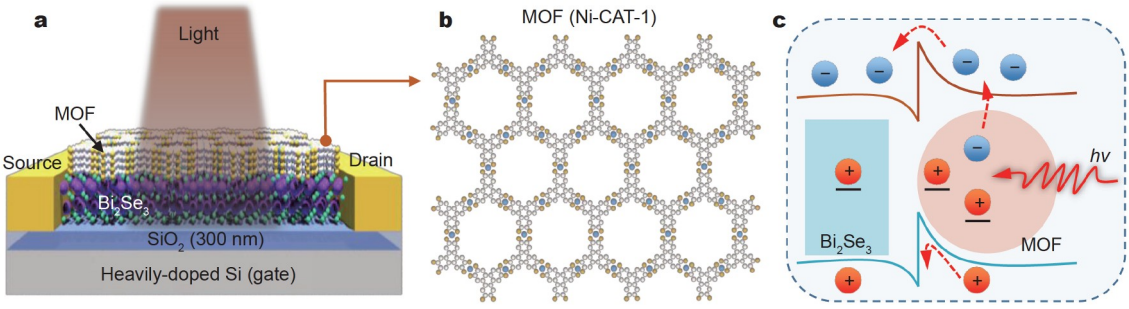

Figure 1 2D Bi_2Se_3/MOF hybrid heterojunction photodetectors. (a) Schematic diagram of the 2D Bi_2Se_3/MOF hybrid heterojunction. (b) Crystal structure of MOF (Ni-CAT-1). (c) Schematic band diagram of the heterojunction photodetector under illumination.

mination. At the same time, photo-generated electron-hole pairs were separated at the interface between the MOF and Bi_2Se_3. The photo-generated electrons were transferred to the Bi_2Se_3 channel to contribute photocurrent. The photo-generated holes remained within the MOF layer as a local gate to regulate the channel conductance, so as to enhance the photoconductivity gain of the device, which thus achieved high performance SWIR photodetection.

The Ni-CAT-1 nanoparticles were synthesized by a simple solution process, in which the HHTP and $Ni(CH_3COO)_2$ stock solutions were used as the precursors (Fig. S1a). As shown in the XRD pattern in Fig. 2b, all diffraction peaks were in good consistence with the simulated peaks, indicating that the as-synthesized Ni-CAT-1 nanoparticles possessed high purity. Moreover, the small full width at half maximum of the XRD peaks demonstrated the high crystallinity of the as-synthesized Ni-CAT-1 nanoparticles. The high-resolution TEM (HRTEM) image shown in Fig. S1b further confirmed the high crystalline quality of the as-synthesized Ni-CAT-1 nanoparticles. Therefore, the simple solution process was further adopted to prepare the 2D Bi_2Se_3/Ni-CAT-1 hybrid heterojunctions. As illustrated in Fig. 2a, the 2D Bi_2Se_3-based device prepared before hand was immersed in the mixture of HHTP and $Ni(CH_3COO)_2$ stock solutions. After heating at 85°C for 12 h, the surface of the 2D

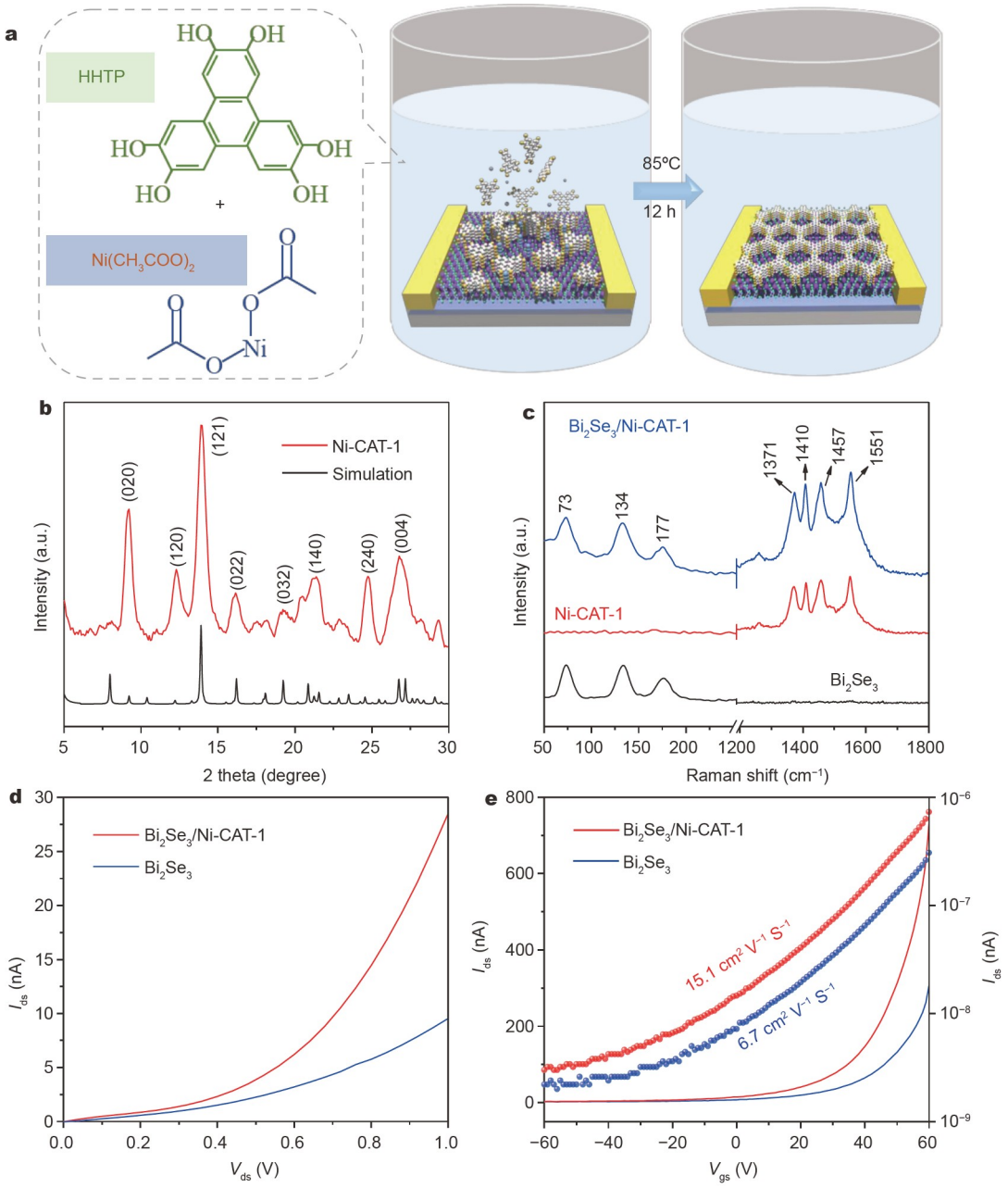

Figure 2 Fabrication and characterization of the 2D Bi_2Se_3/Ni-CAT-1 hybrid heterojunction. (a) Epitaxial growth of Ni-CAT-1 nanoparticles on multilayer Bi_2Se_3 flakes in a sealed glass tube with ethanol solution. (b) XRD patterns of the as-synthesized Ni-CAT-1 nanoparticles. (c) Raman spectra of the Bi_2Se_3 flake and Bi_2Se_3/Ni-CAT-1 hybrid heterojunction. (d) Output characteristic curves of the pristine Bi_2Se_3 and Bi_2Se_3/Ni-CAT-1 hybrid heterojunction at V_{gs} = 0 V. (e) Transfer characteristic curves of the pristine Bi_2Se_3 and Bi_2Se_3/Ni-CAT-1 hybrid heterojunction at V_{ds} = 1 V.

Bi_2Se_3 flakes was covered with a thin film composed of Ni-CAT-1 nanoparticles, thus forming the 2D Bi_2Se_3/Ni-CAT-1 hybrid heterojunctions. Details concerning the experimental process are provided in the EXPERIMENTAL SECTION. Fig. S2a shows an optical microscopic image of the 2D Bi_2Se_3-based device before and after growing Ni-CAT-1 nanoparticles. Obviously, the morphology and structure of the 2D Bi_2Se_3 channel still maintained its integrity, indicating that the preparation process was relatively mild and did not cause damage to the 2D Bi_2Se_3 channel, which ensured the electrical and optoelectronic measurements of the 2D Bi_2Se_3/Ni-CAT-1 hybrid heterojunction devices. The SEM image shown in Fig. S2b indicated that the Ni-CAT-1 nanoparticles were uniformly covered on the surface of the 2D Bi_2Se_3 flakes. According to Fig. S1b, the size of these particles was on the order of nanometers. The thickness of the Ni-CAT-1 nanoparticles thin film was determined to be ~140 nm (Fig. S2b) by AFM. Fig. 2c presents the Raman spectra of the 2D Bi_2Se_3 flakes, Ni-CAT-1 nanoparticles and Bi_2Se_3/Ni-CAT-1 hybrid heterojunctions. Additionally, three peaks located at 73, 134, and 177 cm^{-1} were found in the 2D Bi_2Se_3 flakes, which were assigned to the A^1_{1g}, E^2_g, and A^2_{1g} modes, respectively [32,33]. Four peaks at 1371, 1410, 1457, 1551 cm^{-1} were observed on Ni-CAT-1 nanoparticles, and attributed to the vibrations of C–C bonds of HHTP linkers in Ni-CAT-1 [29,34]. Regarding the Bi_2Se_3/Ni-CAT-1 hybrid heterojunction, the peaks of Bi_2Se_3 and Ni-CAT-1 were observed, revealing that the successful combination of the Ni-CAT-1 nanoparticles on the 2D Bi_2Se_3 flakes.

The electrical characteristics of the pristine 2D Bi_2Se_3 flake and 2D Bi_2Se_3/Ni-CAT-1 hybrid heterojunction were measured in the configuration of back-gate field-effect transistor. Fig. 2d illustrates the output characteristic curves (drain current, I_{ds} *vs.* drain voltage, V_{ds}) of the Bi_2Se_3 and Bi_2Se_3/Ni-CAT-1 hybrid heterojunction in the dark. Obviously, the value of drain current for the Bi_2Se_3/Ni-CAT-1 hybrid heterojunction was higher than that of the pristine 2D Bi_2Se_3 flake. In the meanwhile, the pristine Ni-CAT-1 nanoparticles did not exhibit noticeable electrical conductivity, as shown in Fig. S3. Therefore, the main conducting channel was ascribed to the 2D Bi_2Se_3 flake in the Bi_2Se_3/Ni-CAT-1 hybrid heterojunction device. The increased electrical conductivity in the Bi_2Se_3/Ni-CAT-1 hybrid heterojunction might be caused by the electronic doping of Ni-CAT-1 to Bi_2Se_3. In addition, the transfer characteristic curves (drain current, I_{ds} *vs.* gate voltage, V_{gs}) shown in Fig. 2e also presented an increase in the drain current of the Bi_2Se_3/Ni-CAT-1 hybrid heterojunction in comparison with that of the pristine Bi_2Se_3 device. The log-scale curves in Fig. 2e indicated that the on/off current ratio of the Bi_2Se_3/Ni-CAT-1 hybrid heterojunction slightly increased from 139 to 244. The electrical characteristics revealed that the electronic doping effect occurred in the 2D Bi_2Se_3 flake after the combination of the Ni-CAT-1 nanoparticles, which was in accordance with the previously reported results in graphene/Ni-CAT-1 structure [29]. The field-effect mobility (μ) of the pristine 2D Bi_2Se_3 flakes and Bi_2Se_3/Ni-CAT-1 hybrid heterojunction was evaluated by the equation [35]: $\mu = (\Delta I_{ds}/\Delta I_{gs})(L/WC_{ox}V_{ds})$, where L, W and C_{ox} represent the channel length, width and gate capacitance, respectively. As a result, the field-effect mobility of the pristine Bi_2Se_3 and Bi_2Se_3/Ni-CAT-1 hybrid heterojunction was calculated to be 6.7 and 15.1 $cm^2 V^{-1} s^{-1}$, respectively. This enhancement (by ~2 times) of field-effect mobility in the Bi_2Se_3/Ni-CAT-1 hybrid heterojunction was due to the possible electronic doping effect [36].

Before evaluating the enhancement of the photodetection performance of the Bi_2Se_3/Ni-CAT-1 hybrid heterojunction compared with that of the pristine Bi_2Se_3, the optical absorption properties of the device before and after Ni-CAT-1 nanoparticles hybridization were investigated in this study. According to Fig. 3a, the pristine Bi_2Se_3 exhibited a certain light absorption capacity within the range of 500–1500 nm. However its absorption in the range of 1500–2500 nm was weak, while the Ni-CAT-1 nanoparticles demonstrated a better absorption capacity than that of the pristine Bi_2Se_3 in the range of 500–2500 nm. When the Ni-CAT-1 nanoparticles were grown onto the Bi_2Se_3 channel, the Bi_2Se_3/Ni-CAT-1 hybrid heterojunction exhibited enhanced absorption from 500 to 2500 nm, which was ascribed to the synergetic absorption effect of Ni-CAT-1 nanoparticles and Bi_2Se_3 flake. Moreover, the Bi_2Se_3/Ni-CAT-1 hybrid heterojunction presented a strong absorption peak at around 1500 nm, which was absent in the individual 2D Bi_2Se_3 flake and Ni-CAT-1 nanoparticles. This phenomenon may be caused by the energy transfer between Bi_2Se_3 and Ni-CAT-1 [37]. The enhanced absorption and possible energy transfer enabled the Bi_2Se_3/Ni-CAT-1 hybrid heterojunction as the high-performance broadband photodetector.

Then, we concentrated our efforts on the photoelectric performance of the Bi_2Se_3/Ni-CAT-1 hybrid heterojunction device. Fig. 3b, c show the photoelectric properties of the pristine Bi_2Se_3 and Bi_2Se_3/Ni-CAT-1 hybrid heterojunction under illumination with various wavelengths ranging from 500 to 2000 nm, respectively. Based on the curves in Fig. 3b, the pristine 2D Bi_2Se_3 flake exhibited an obvious photo-response in the spectral range of 500–1600 nm, yet had a weak response in the near-infrared region with the wavelength of 1000–1600 nm due to its weak light absorption. Under the same light irradiation condition, the 2D Bi_2Se_3/Ni-CAT-1 hybrid heterojunction showed stronger photo-response than the pristine 2D Bi_2Se_3 flake (Fig. 3c) because of its higher light absorption. In addition, on account of the broad spectral absorption of Ni-CAT-1 nanoparticles, the photo-response range of the Bi_2Se_3/Ni-CAT-1 hybrid heterojunction was extended to 2000 nm, which was difficult to be achieved in a single 2D Bi_2Se_3-based photodetector [33,38]. Fig. S4 displays the photo-response switching of the Bi_2Se_3/Ni-CAT-1 hybrid heterojunction under illumination at 500, 1000, 1500, and 2000 nm, respectively, indicating the highly reproducible and stable photo-response properties. These results further demonstrated that the Ni-CAT-1 nanoparticles hybridization not only enhanced the photodetection performance of the 2D Bi_2Se_3 flake, but also broadened its photodetection range.

To better understand the performance improvement of the device based on the 2D Bi_2Se_3 flake by Ni-CAT-1 nanoparticles hybridization, the photocurrent (I_{ph}), responsivity (R), and detectivity (D^*) of the pristine Bi_2Se_3 and Bi_2Se_3/Ni-CAT-1 hybrid heterojunction were systematically studied under different excitation wavelengths. R and D^* denote two important characteristic parameters to evaluate the performance of a photodetector, representing the ability of generating photocurrent under illumination and detecting minimum illumination signal, respectively. The calculation formula is expressed as follows [39]: $I_{ph} = I_{illuminated} - I_{dark}$, $R = I_{ph}/(PS)$, $D^* = R(S/2eI_{dark})^{1/2}$, where the $I_{illuminated}$, I_{dark}, P, S, and e refer to the device current under illumination, dark current, power density of incident light, device effective area, and elementary electronic

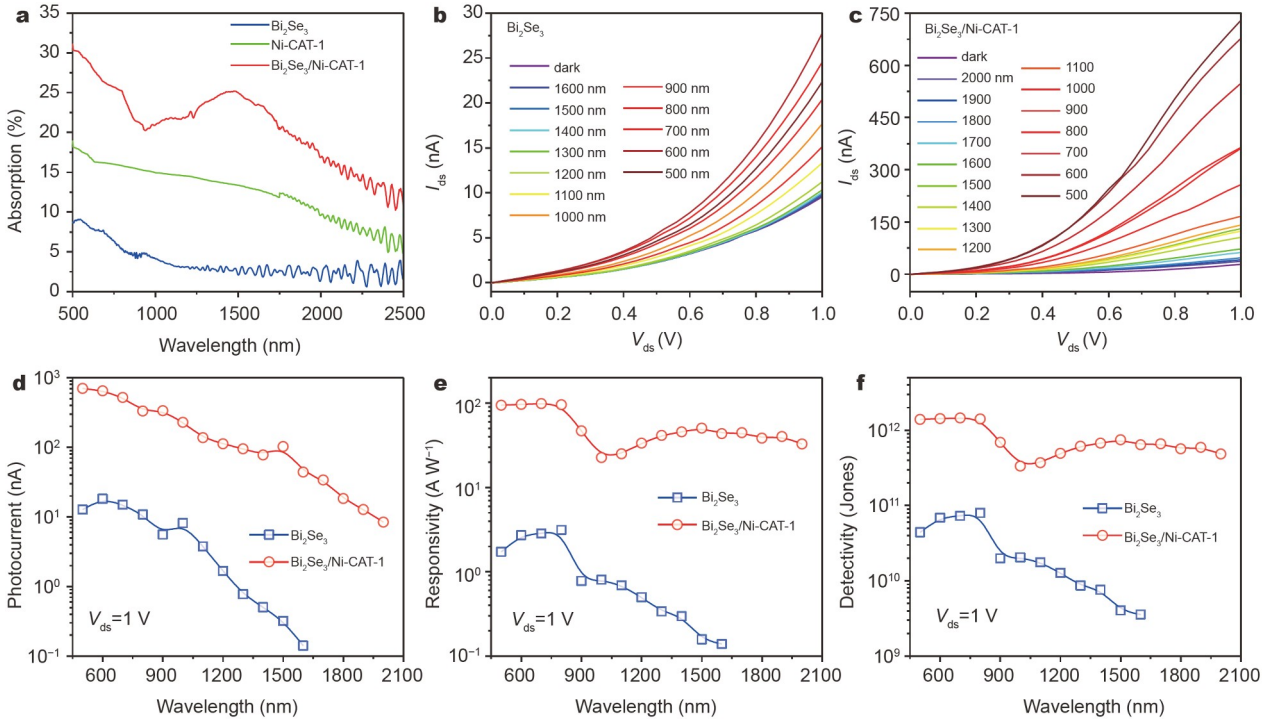

Figure 3 Broadband photodetection performance of the pristine 2D Bi_2Se_3 flake and 2D Bi_2Se_3/Ni-CAT-1 hybrid heterojunction. (a) Optical absorption spectra of the pristine Bi_2Se_3, Ni-CAT-1 nanoparticles and Bi_2Se_3/Ni-CAT-1 hybrid heterojunction. (b) I_{ds}-V_{ds} curves of the pristine Bi_2Se_3 device in the dark and under illumination with various wavelengths ranging from 500 to 1600 nm. (c) I_{ds}-V_{ds} curves of the Bi_2Se_3/Ni-CAT-1 hybrid heterojunction in the dark and under illumination with various wavelengths ranging from 500 to 2000 nm. (d) Photocurrent, (e) responsivity and (f) detectivity of the Bi_2Se_3 devices with and without Ni-CAT-1 nanoparticles hybridization at wavelengths from 500 to 2000 nm, respectively.

charge, respectively. Fig. 3d shows the I_{ph} actually obtained from Fig. 3b, c under different wavelengths, while Fig. 3e, f present the calculated R and D^* based on Fig. 3d. Clearly, the photocurrent of the Bi_2Se_3/Ni-CAT-1 hybrid heterojunction under excitation at different wavelengths was 2–3 orders of magnitude higher than that of the pristine Bi_2Se_3, indicating that hybridization is an extremely effective strategy to improve the photodetection performance of the 2D Bi_2Se_3 flake. Regarding the Bi_2Se_3/Ni-CAT-1 hybrid heterojunction, the R values were calculated to be 94.5, 22.6, 50.5, and 32.8 A W^{-1} at 500, 1000, 1500, and 2000 nm, respectively. Comparatively, the pristine 2D Bi_2Se_3 flake exhibited much smaller R values of 1.7, 0.8, and 0.14 A W^{-1} at 500, 1000, and 1500 nm, respectively. Similarly, the D^* of the Bi_2Se_3/Ni-CAT-1 hybrid heterojunction reached up to 1.4×10^{12}, 3.3×10^{11}, 7.5×10^{11}, and 4.8×10^{11} Jones at 500, 1000, 1500, and 2000 nm, respectively, which were much higher than that of the pristine 2D Bi_2Se_3 flake (4.4×10^{10} Jones at 500 nm, 2.1×10^{10} Jones at 1000 nm and 4.1×10^{9} Jones at 1500 nm). In addition, the EQE values of the pristine 2D Bi_2Se_3 flake and Bi_2Se_3/Ni-CAT-1 hybrid heterojunction were estimated by the following formula: EQE = $hcR/e\lambda$, where h, c, e, λ and R refer to the Planck constant, light velocity, elementary electronic charge, incident wavelength and responsivity, respectively. The as-estimated EQE values of the Bi_2Se_3/Ni-CAT-1 hybrid heterojunction were 23,495%, 2809% and 4185% at 500, 1000 and 1500 nm, higher than that of the pristine 2D Bi_2Se_3 flake (423%/99%/11% at 500/1000/1500 nm). Briefly, the Bi_2Se_3/Ni-CAT-1 hybrid heterojunction photodetector demonstrated an overall improvement in the aspect of photocurrent, responsivity, detectivity and EQE compared with the pristine Bi_2Se_3.

From the above analyses, the Bi_2Se_3/Ni-CAT-1 hybrid heterojunction exhibited a superior photodetection performance at 1500 nm compared with the pristine Bi_2Se_3. Thus, the excitation wavelength used in the following studies was set to 1500 nm. Fig. 4a displays the output characteristic curves of the Bi_2Se_3/Ni-CAT-1 hybrid heterojunction under 1500 nm illumination with various power densities (from 0.012 to 1.012 mW cm^{-2}). The drain current monotonically increased with the increasing power density. The photocurrent as a function of power density at V_{ds} = 1 V was plotted in Fig. 4b, which was fitted in a simple power law $I_{ph} \sim P^{\alpha}$. The α is a constant related to the generation, trapping and recombination of photo-generated carriers. The fitted α is 0.38, indicating the presence of trap-assisted photo-generated electron-hole pairs recombination at the interface of the Bi_2Se_3/Ni-CAT-1 hybrid heterojunction [40,41]. Additionally, the responsivity as a function of power density was plotted in Fig. 4c. The obtained maximum responsivity was calculated to be 395 A W^{-1} at a low incident power density of 0.012 mW cm^{-2}. Moreover, the photo-response switching of the Bi_2Se_3/Ni-CAT-1 hybrid heterojunction exhibited good stability, which was found in Fig. S5. Through careful analysis of one of the cycles, it was found that the Bi_2Se_3/Ni-CAT-1 hybrid heterojunction exhibited a fast photo-response rate. According to Fig. 4d, the rising time (τ_{rising}) and decay time (τ_{decay}) of the heterojunction were ~130 and ~6 ms, respectively, faster than those of the individual Bi_2Se_3 device (τ_{rising} ~0.54 s, τ_{decay} ~0.47 s) [33]. The fast photo-response rate in the Bi_2Se_3/Ni-CAT-1 hybrid heterojunction was possibly attributed to the Schottky contact at the electrode/Bi_2Se_3 interface, as inferred from the non-linear I_{ds}-V_{ds} curves. The Schottky barrier efficiently promoted the separation of photo-generated

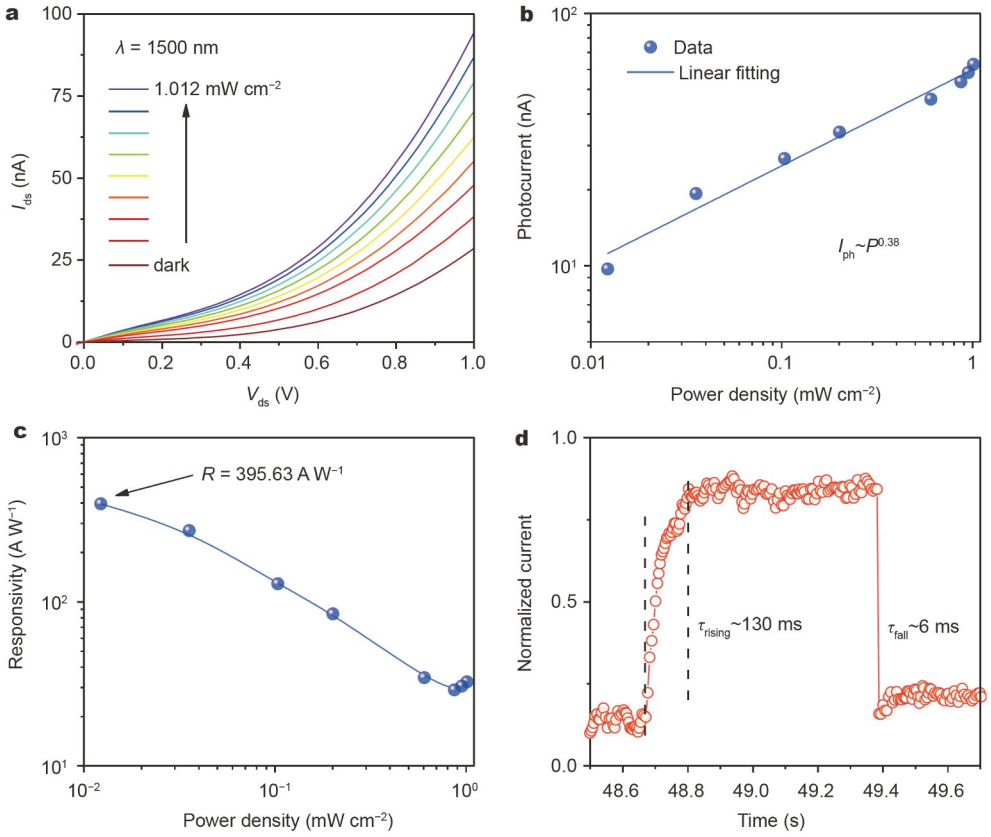

Figure 4 Photoresponse properties of the Bi_2Se_3/Ni-CAT-1 hybrid heterojunction under 1500 nm illumination. (a) I_{ds}-V_{ds} curves of the Bi_2Se_3/Ni-CAT-1 hybrid heterojunction in the dark and under illumination with various power densities ranging from 0.012 to 1.012 mW cm^{-2}. (b, c) Light-power-dependent photocurrent and responsivity at V_{ds} = 1 V. (d) Response rate of the Bi_2Se_3/Ni-CAT-1 hybrid heterojunction with a rising time of 130 ms and a decay time of 6 ms.

electron-hole pairs, leading to a fast photo-response dynamics [14,42].

To explore the possible photo-response mechanism in the Bi_2Se_3/Ni-CAT-1 hybrid heterojunction, the gate-modulated photo-response was further investigated in detail. The transfer characteristic curves of the Bi_2Se_3/Ni-CAT-1 hybrid heterojunction in dark and under 1500 nm illumination with various power densities are illustrated in Fig. 5a. The drain current of the heterojunction increased with the increasing power density in the gate voltage range of −60–60 V. In addition, the Bi_2Se_3/Ni-CAT-1 hybrid heterojunction presented a stable and repeatable photo-response under 1500 nm illumination with a power density of 1.012 mW cm^{-2} at V_{ds} = 1 V and V_{gs} = 0 V (Fig. 5b). Fig. 5c depicts the power density dependence of photocurrent at different gate voltages, which were fitted by the power law of $I_{ph} \sim P^{\alpha}$. Regarding a photodetector, the α value is related to the two photo-response mechanisms of photogating effect ($\alpha < 1$) and photoconductive effect ($\alpha \approx 1$) [43,44]. The α values of the Bi_2Se_3/Ni-CAT-1 hybrid heterojunction at different gate voltages are displayed in Fig. 5d. Therefore, it was found that the obtained α value varied from 0.26 to 0.41 in the gate voltage range from −60 to 60 V, much smaller than 1, manifesting that the photogating effect was the dominating photo-response mechanism. Under the photogating effect, the photo-generated electrons in the Bi_2Se_3/Ni-CAT-1 hybrid heterojunction circulated multiple times in the channel due to the modulation of the charged trap states, resulting in a high photoconductive gain (G). [45,46] The G can be estimated by the equation [39]: $G = \tau_{life}/\tau_{tran}$, where the τ_{life} and τ_{tran} are the lifetime of photo-generated carriers and the drift transit time of carriers, respectively. The lifetime (τ_{life}) could be presented by the response time (~6 ms) and the transit time (τ_{tran}) was written as [39]: $\tau_{tran} = L^2/(\mu V_{bias})$, where L, μ and V_{bias} refer to the channel length, carrier mobility and bias voltage, respectively. The calculated G reached up to 6.3 × 10^4, indicating that high photodetection performance was obtained in the Bi_2Se_3/Ni-CAT-1 hybrid heterojunction.

Fig. 5e, f demonstrate gate-modulated responsivity and detectivity of the Bi_2Se_3/Ni-CAT-1 hybrid heterojunction, which increased sharply with the increase of the applied gate voltage. The behavior was explained by a gate-modulated energy band structure [17,36]. Under the equilibrium conditions of no illumination and gate voltage, the photoelectrical properties were mainly affected by the Schottky barrier at the contact interface (Fig. 5g). The Schottky barrier significantly increased at the negative gate voltage, leading to negligible thermionic and tunneling current. As a result, the channel current was contributed by the photo-generated carriers of Bi_2Se_3 and Ni-CAT-1 under illumination (Fig. 5h). Under positive gate voltage, in addition to the photo-generated current, the thermionic and tunneling current gradually increased as a result of decreasing Schottky barrier height, thus forming a significantly increased channel current (Fig. 5i). Therefore, on account of the synergistic effect of tunable Schottky barrier and photogating mechanism, the channel current remarkably increased at the positive gate vol-

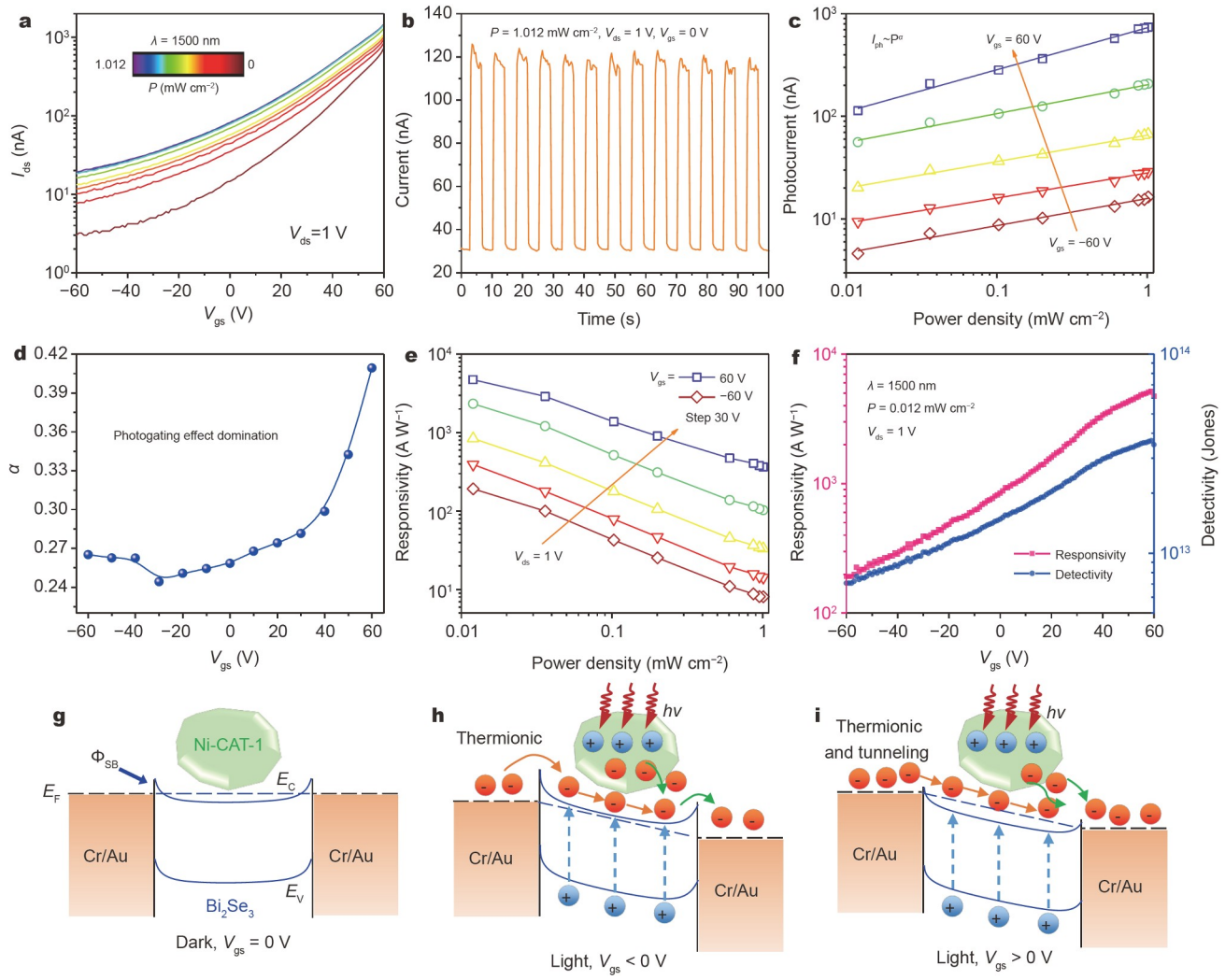

Figure 5 Gate-modulated photodetection performance of the Bi_2Se_3/Ni-CAT-1 hybrid heterojunction under illumination at 1500 nm. (a) Transfer characteristic curves of the Bi_2Se_3/Ni-CAT-1 hybrid heterojunction in the dark and under 1500 nm illumination with various power densities ranging from 0.012 to 1.012 mW cm^{-2}. (b) Time-resolved photoresponse at a power density of 1.012 mW cm^{-2}, V_{ds} = 1 V and V_{gs} = 0 V. (c) Power-dependent photocurrent at different gate voltages. (d) Exponent (α) extracted from (c) for each gate voltage. (e) Light-power-dependent responsivity at different gate voltages. (f) Responsivity and detectivity as a function of gate voltage. The carrier transport mechanism and band energy diagram of the Bi_2Se_3/Ni-CAT-1 hybrid heterojunction at (g) equilibrium state, (h) V_{gs} < 0 V, and (i) V_{gs} > 0 V.

Table 1 Comparison of photodetection performance between the Bi_2Se_3/Ni-CAT hybrid heterojunction and other photodetectors with similar structure

Device	Wavelength (nm)	Bias (V)	Responsivity (A W^{-1})	Detectivity (Jones)	Response rate	Ref.
Bi_2Se_3/Ni-CAT-1	1500	V_{ds} = 1 V_{gs} = 60	4725	3.5 × 10^{13}	130/6 ms	This work
Bi_2Se_3/MoO_3	1550	V_{ds} = 20	739	~3 × 10^{10}	62/76 μs	[2]
Bi_2Te_3/pentacene	1550	V_{ds} = 0	~1	~10^{9}	3.26/5.07 ms	[47]
Graphene/HgTe	2500	V_{ds} = 1 V_{gs} = −2.5	6.5 × 10^{-3}	~ 10^{9}	10^{-5} s	[48]
MoS_2/PbS	1200	V_{ds} = 2	0.543	2.68 × 10^{12}	–	[49]
MoS_2/$CuInSe_2$	1064	V_{ds} = 1 V_{gs} = 60	74.8	7.1 × 10^{11}	1.5/1.2 s	[36]
Ge/Perovskite	980	V_{ds} = 1	32	2.2 × 10^{9}	2.1/5.7 ms	[50]

tage, causing the high photodetection performance. Obviously, the Bi_2Se_3/Ni-CAT-1 hybrid heterojunction reached a responsivity of 4725 A W^{-1} and a detectivity of 3.5 × 10^{13} Jones at V_{gs} = 60 V. Based on Table 1, the present device performance of

Bi_2Se_3/Ni-CAT-1 is superior to that of the reported photodetectors with similar structure.

CONCLUSIONS

To conclude, a high-performance infrared photodetector based on 2D Bi_2Se_3 flakes was fabricated with the hybridization of MOF (Ni-CAT-1) nanoparticles through a simple solution process. Benefiting from the strong optical absorption of MOF (Ni-CAT-1) nanoparticles and the high carrier mobility of 2D Bi_2Se_3 flake, the Bi_2Se_3/MOF hybrid heterojunction demonstrated excellent photo-response performance in the wavelength range of 500–2000 nm, with 2–3 orders of magnitude higher than that of the pristine Bi_2Se_3-based photodetector. Specifically, an outstanding responsivity of 4725 A W^{-1} and a high detectivity of 3.5×10^{13} Jones were achieved at 1500 nm due to the synergistic effect of photogating effect and the gate-modulated Schottky barrier. These results demonstrated the potential of MOF nanomaterials in enhancing the photodetection performance of photodetectors based on 2D layered materials.

Received 26 July 2021; accepted 27 August 2021; published online 29 September 2021

1 Guan X, Yu X, Periyanagounder D, *et al.* Recent progress in short- to long-wave infrared photodetection using 2D materials and heterostructures. Adv Opt Mater, 2020, 9: 2001708
2 Yang M, Han Q, Liu X, *et al.* Ultrahigh stability 3D TI Bi_2Se_3/MoO_3 thin film heterojunction infrared photodetector at optical communication waveband. Adv Funct Mater, 2020, 30: 1909659
3 Tan C, Amani M, Zhao C, *et al.* Evaporated Se_xTe_{1-x} thin films with tunable bandgaps for short-wave infrared photodetectors. Adv Mater, 2020, 32: 2001329
4 Wang P, Xia H, Li Q, *et al.* Sensing infrared photons at room temperature: From bulk materials to atomic layers. Small, 2019, 15: 1904396
5 Wang F, Zhang Y, Gao Y, *et al.* 2D metal chalcogenides for IR photodetection. Small, 2019, 15: 1901347
6 Tong L, Peng M, Wu P, *et al.* Hole-dominated Fowler-Nordheim tunneling in 2D heterojunctions for infrared imaging. Sci Bull, 2021, 66: 139–146
7 Liu J, Xia F, Xiao D, *et al.* Semimetals for high-performance photodetection. Nat Mater, 2020, 19: 830–837
8 Wang F, Pei K, Li Y, *et al.* 2D homojunctions for electronics and optoelectronics. Adv Mater, 2021, 33: 2005303
9 Liu R, Wang F, Liu L, *et al.* Band alignment engineering in two-dimensional transition metal dichalcogenide-based heterostructures for photodetectors. Small Struct, 2020, 2: 2000136
10 Liu L, Zhai T. Wafer-scale vertical van der Waals heterostructures. InfoMat, 2020, 3: 3–21
11 Guo Z, Cao R, Wang H, *et al.* High performance polarization sensitive photodetectors on two-dimensional β-InSe. Natl Sci Rev, 2021, doi: 10.1093/nsr/nwab098
12 Konstantatos G, Badioli M, Gaudreau L, *et al.* Hybrid graphene-quantum dot phototransistors with ultrahigh gain. Nat Nanotech, 2012, 7: 363–368
13 Chen Z, Li X, Wang J, *et al.* Synergistic effects of plasmonics and electron trapping in graphene short-wave infrared photodetectors with ultrahigh responsivity. ACS Nano, 2017, 11: 430–437
14 Dai M, Chen H, Feng R, *et al.* A dual-band multilayer InSe self-powered photodetector with high performance induced by surface plasmon resonance and asymmetric Schottky junction. ACS Nano, 2018, 12: 8739–8747
15 Huo N, Gupta S, Konstantatos G. MoS_2-HgTe quantum dot hybrid photodetectors beyond 2 μm. Adv Mater, 2017, 29: 1606576
16 Luo P, Zhuge F, Wang F, *et al.* PbSe quantum dots sensitized high-mobility Bi_2O_2Se nanosheets for high-performance and broadband photodetection beyond 2 μm. ACS Nano, 2019, 13: 9028–9037
17 Wu H, Si H, Zhang Z, *et al.* All-inorganic perovskite quantum dot-monolayer MoS_2 mixed-dimensional van der Waals heterostructure for ultrasensitive photodetector. Adv Sci, 2018, 5: 1801219
18 Wang L, Zou X, Lin J, *et al.* Perovskite/black phosphorus/MoS_2 photogate reversed photodiodes with ultrahigh light on/off ratio and fast response. ACS Nano, 2019, 13: 4804–4813
19 Yang T, Wang X, Zheng B, *et al.* Ultrahigh-performance optoelectronics demonstrated in ultrathin perovskite-based vertical semiconductor heterostructures. ACS Nano, 2019, 13: 7996–8003
20 Yu X, Li Y, Hu X, *et al.* Narrow bandgap oxide nanoparticles coupled with graphene for high performance mid-infrared photodetection. Nat Commun, 2018, 9: 4299
21 Zhou N, Xu B, Gan L, *et al.* Narrowband spectrally selective near-infrared photodetector based on up-conversion nanoparticles used in a 2D hybrid device. J Mater Chem C, 2017, 5: 1591–1595
22 Dong R, Han P, Arora H, *et al.* High-mobility band-like charge transport in a semiconducting two-dimensional metal-organic framework. Nat Mater, 2018, 17: 1027–1032
23 Bera KP, Haider G, Usman M, *et al.* Trapped photons induced ultrahigh external quantum efficiency and photoresponsivity in hybrid graphene/metal-organic framework broadband wearable photodetectors. Adv Funct Mater, 2018, 28: 1804802
24 Arora H, Dong R, Venanzi T, *et al.* Demonstration of a broadband photodetector based on a two-dimensional metal-organic framework. Adv Mater, 2020, 32: 1907063
25 Liang B, Lin RB, Chen B. Emerging 2D functional metal-organic framework materials. Natl Sci Rev, 2020, 7: 3–5
26 Ma Y, Lu Y, Hai G, *et al.* Bidentate carboxylate linked TiO_2 with NH_2-MIL-101(Fe) photocatalyst: A conjugation effect platform for high photocatalytic activity under visible light irradiation. Sci Bull, 2020, 65: 658–669
27 Wang L, Jin P, Duan S, *et al. In-situ* incorporation of copper(II) porphyrin functionalized zirconium MOF and TiO_2 for efficient photocatalytic CO_2 reduction. Sci Bull, 2019, 64: 926–933
28 Yan ZH, Ma B, Li SR, *et al.* Encapsulating a Ni(II) molecular catalyst in photoactive metal-organic framework for highly efficient photoreduction of CO_2. Sci Bull, 2019, 64: 976–985
29 Wu J, Chen J, Wang C, *et al.* Metal-organic framework for transparent electronics. Adv Sci, 2020, 7: 1903003
30 Allendorf MD, Dong R, Feng X, *et al.* Electronic devices using open framework materials. Chem Rev, 2020, 120: 8581–8640
31 Wang F, Luo P, Zhang Y, *et al.* Band structure engineered tunneling heterostructures for high-performance visible and near-infrared photodetection. Sci China Mater, 2020, 63: 1537–1547
32 Zhang J, Peng Z, Soni A, *et al.* Raman spectroscopy of few-quintuple layer topological insulator Bi_2Se_3 nanoplatelets. Nano Lett, 2011, 11: 2407–2414
33 Wang F, Li L, Huang W, *et al.* Submillimeter 2D Bi_2Se_3 flakes toward high-performance infrared photodetection at optical communication wavelength. Adv Funct Mater, 2018, 28: 1802707
34 Shao F, Dai W, Zhang Y, *et al.* Chemical mapping of nanodefects within 2D covalent monolayers by tip-enhanced Raman spectroscopy. ACS Nano, 2018, 12: 5021–5029
35 Sun X, Zhu C, Liu H, *et al.* Contact and injection engineering for low SS reconfigurable FETs and high gain complementary inverters. Sci Bull, 2020, 65: 2007–2013
36 Shen T, Li F, Zhang Z, *et al.* High-performance broadband photodetector based on monolayer MoS_2 hybridized with environment-friendly $CuInSe_2$ quantum dots. ACS Appl Mater Interfaces, 2020, 12: 54927–54935
37 Iqbal MA, Liaqat A, Hussain S, *et al.* Ultralow-transition-energy organic complex on graphene for high-performance shortwave infrared photodetection. Adv Mater, 2020, 32: 2002628
38 Liu JL, Chen H, Li X, *et al.* Ultra-fast and high flexibility near-infrared photodetectors based on Bi_2Se_3 nanobelts grown *via* catalyst-free van der Waals epitaxy. J Alloys Compd, 2020, 818: 152819
39 Long M, Wang P, Fang H, *et al.* Progress, challenges, and opportunities for 2D material based photodetectors. Adv Funct Mater, 2019, 29:

1803807
40 Hu C, Dong D, Yang X, *et al.* Synergistic effect of hybrid PbS quantum dots/2D-WSe_2 toward high performance and broadband photodetectors. Adv Funct Mater, 2017, 27: 1603605
41 Zhang Y, Wang J, Wang B, *et al.* Extending the spectral responsivity of MoS_2 phototransistors by incorporating up-conversion microcrystals. Adv Opt Mater, 2018, 6: 1800660
42 Dai M, Chen H, Wang F, *et al.* Ultrafast and sensitive self-powered photodetector featuring self-limited depletion region and fully depleted channel with van der Waals contacts. ACS Nano, 2020, 14: 9098–9106
43 Wang F, Zhang Z, Zhang Y, *et al.* Honeycomb RhI_3 flakes with high environmental stability for optoelectronics. Adv Mater, 2020, 32: 2001979
44 Island JO, Blanter SI, Buscema M, *et al.* Gate controlled photocurrent generation mechanisms in high-gain In_2Se_3 phototransistors. Nano Lett, 2015, 15: 7853–7858
45 Li L, Wang W, Chai Y, *et al.* Few-layered PtS_2 phototransistor on h-BN with high gain. Adv Funct Mater, 2017, 27: 1701011
46 Zhang YJ, Ye JT, Yomogida Y, *et al.* Formation of a stable p-n junction in a liquid-gated MoS_2 ambipolar transistor. Nano Lett, 2013, 13: 3023–3028
47 Yang M, Wang J, Zhao Y, *et al.* Three-dimensional topological insulator Bi_2Te_3/organic thin film heterojunction photodetector with fast and wideband response from 450 to 3500 nanometers. ACS Nano, 2019, 13: 755–763
48 Noumbé UN, Gréboval C, Livache C, *et al.* Reconfigurable 2D/0D p-n graphene/HgTe nanocrystal heterostructure for infrared detection. ACS Nano, 2020, 14: 4567–4576
49 Mukherjee S, Jana S, Sinha TK, *et al.* Infrared tunable, two colour-band photodetectors on flexible platforms using 0D/2D PbS-MoS_2 hybrids. Nanoscale Adv, 2019, 1: 3279–3287
50 Hu W, Cong H, Huang W, *et al.* Germanium/perovskite heterostructure for high-performance and broadband photodetector from visible to infrared telecommunication band. Light Sci Appl, 2019, 8: 106

Acknowledgements This work was supported by the National Natural Science Foundation of China (21825103 and 51727809), the Natural Science Foundation of Hubei Province (2019CFA002), the Fundamental Research Funds for the Central Universities (2019kfyXMBZ018) and China Postdoctoral Science Foundation (2021M691108). The authors thank the Analytical and Testing Centre of Huazhong University of Science and Technology.

Author contributions Wang F and Zhang N performed the growth of 2D Bi_2Se_3 flakes. Wang F and Wu J fabricated the Bi_2Se_3/Ni-CAT-1 hybrid heterojunctions. Zhang Y did the AFM measurement. Wang F performed the properties characterization, device tests and manuscript writing. Zhai T supervised the project. Wang F, Yang S, Li H and Zhai T discussed the manuscript and revision.

Conflict of interest The authors declare that they have no conflict of interest.

Supplementary information Supporting data are available in the online version of the paper.

Fakun Wang received his BSc degree in mineral processing engineering from the Central South University in 2016. He is studying for his PhD degree at Huazhong University and Technology (HUST) under the supervision of Professor Tianyou Zhai. His work focuses on the controllable synthesis of low-dimensional inorganic materials, and their promising applications in optoelectronics.

Tianyou Zhai received his BSc degree in chemistry from Zhengzhou University in 2003, and PhD degree in physical chemistry from the Institute of Chemistry, Chinese Academy of Sciences (ICCAS) under the supervision of Prof. Jiannian Yao in 2008. Afterwards he joined in the National Institute for Materials Science (NIMS) as a postdoctoral fellow of Japan Society for the Promotion of Science (JSPS) in Prof. Yoshio Bando's group and then as a researcher of the International Center for Young Scientists (ICYS) within NIMS. Currently, he is a chief professor of the School of Materials Science and Engineering, HUST. His research interests include the controlled synthesis and exploration of fundamental physical properties of inorganic functional nanomaterials, as well as their promising applications in energy science, electronics and optoelectronics.

金属有机框架集成二维层状材料用于高性能短波红外光探测

王发坤, 吴洁, 张悦, 杨思捷, 张娜, 李会巧, 翟天佑*

摘要 工作在短波红外区域的光电探测器因其在商业和军事领域的广泛应用而备受重视, 窄带隙二维层状材料(2DLM)被认为是构筑下一代高性能红外光电探测器的潜在候选者. 然而, 这类材料在原子级厚度时光吸收较弱, 致使其探测性能难以满足实际需求. 在本文中, 我们提出了一种通过集成具有优异光吸收特性的金属有机骨架(MOF)纳米粒子和高迁移率的2DLM来设计高性能短波红外光电探测器的策略, 并通过构筑MOF/2DLM(Ni-CAT-1/Bi_2Se_3)混合异质结光电探测器演示了该策略的可行性. 由于光生载流子从MOF转移到Bi_2Se_3, 集成在Bi_2Se_3层上的MOF纳米颗粒使异质结的光电流增加了2–3个数量级. 该混合异质结光电探测器在1500 nm光照下的响应度和探测度分别达4725 A W^{-1}和3.5×10^{13} Jones. 如此优异性能主要源于增强的光吸收和光门控效应的协同作用. 本文提出的集成MOF光敏材料和2DLM的策略为未来构建高性能短波红外光电探测器提供了思路.

